Chapter 5

Sequential Checkpoints Govern Substrate Selection during Co-translational Protein Targeting

A version of this chapter will be published as a Report in Science on May 7th, 2010

X. Zhang, R. Rashid, K. Wang, and S.-O. Shan, Science, (2010), 328, 757-760.

5.1 Abstract

Proper localization of proteins to their correct cellular destinations is essential for all cells. However, the precise mechanism by which high fidelity is achieved in protein localization is not well understood for any targeting pathways. To probe this fundamental question we investigated targeting of proteins by the signal recognition particle (SRP). The "signal hypothesis" postulates that the signal sequence on a protein allows it to be specifically recognized by targeting factors such as SRP, which mediates the delivery of the protein to the correct cellular compartment. It was generally thought that fidelity arises from the inability of SRP to bind strongly to incorrect cargos. Here we show that incorrect cargos are further rejected through a series of fidelity checkpoints during subsequent steps of targeting, including complex formation between the SRP and SRP receptor (SR) and kinetic proofreading through GTP hydrolysis. Thus the SRP pathway achieves a high fidelity through the cumulative effect of multiple checkpoints; this principle may be generally applicable to other complex cellular pathways that need to recognize degenerate signals or discriminate between correct and incorrect substrates based on minor differences.

5.2 Introduction

Co-translational protein targeting by the SRP is an essential and evolutionarily conserved pathway for delivering proteins to cellular membranes (*2, 96*). SRP recognizes ribosomes translating nascent polypeptide chains (RNCs) as its cargo (figure 5.1A, step 1) (*2, 82, 85, 91, 92, 96*). Cargo loading enables efficient assembly of an SRP•SR complex through interactions between their GTPase domains, and the cargo stabilizes the

GTPase complex in an *early* conformational state (step 2) (*4, 5*). The interactions of SR with the target membrane and the protein conducting channel (PCC) is proposed to induce dynamic rearrangements in the SRP•SR complex (*5, 85, 92*), first to form a GTP-dependent *closed* complex (step 3) and then to activate GTP hydrolysis in the complex (step 4). These rearrangements facilitate the unloading of cargo from SRP to the PCC (steps 3–4) (*5, 85, 92*). In a productive targeting cycle, GTP is hydrolyzed after cargo unloading to drive the disassembly and recycling of SRP and SR (step 5) (*45*).

Despite significant progress in our dissection of the SRP pathway as a paradigm for understanding the molecular basis of protein localization, how the SRP ensures faithful delivery of correct cargos remains poorly understood. Like other topogenic sequences that mediate protein localization, signal sequences that engage the SRP lack a consensus motif and are highly divergent (*97-99*), with a hydrophobic core as their primary distinguishing feature (*98, 100*). Thus the SRP needs to be highly adaptable; indeed it was proposed that the methionine-rich M-domain of SRP provides a flexible pocket to accommodate diverse signal sequences (*15, 101*). Nevertheless, the difference in signal sequences of substrates that engage SRP vs. SRP-independent pathways are relatively minor (*102*). Thus despite its flexibility, the SRP has evolved a strategy to remain highly specific to its substrates. Here we demonstrate that the SRP pathway achieves high fidelity through a combination of binding, induced fit and kinetic proofreading mechanisms.

5.3 Results

It was generally thought that 'incorrect' cargos without strong signal sequences are rejected because they bind weakly to the SRP (figure 5.1A, arrow a). To test this hypothesis, we systematically varied the signal sequence based on alkaline phosphatase (phoA), a 'borderline' substrate targeted by either the SRP or SecB pathway (*102, 103*). We replaced the hydrophobic core of the phoA signal sequence (figure 1B, bold) with a combination of leucine and alanine, and varied the Leu/Ala ratio to generate signal sequences with different hydrophobicity (*103, 104*). As another means to vary the signal sequence and generate an incorrect cargo, the *E. coli* autotransporter EspP was used. Although the EspP signal peptide has a hydrophobicity comparable to that of phoA-3A7L, EspP enters the PCC via an SRP-independent pathway due to the presence of an N-terminal signal peptide extension (figure 5.1B, blue) (*105*). Firefly luciferase, a cytosolic protein without any identifiable signal sequences, was used as a negative control (figure 5.1B) (*103*). For all the following experiments, homogeneous stalled RNCs were purified and used as cargos (*5, 67*).

We first tested the binding affinities of SRP for different cargos. A single cysteine was engineered into the SRP M-domain (C421) and labeled with 5-maleimide-fluorescein (F5M); RNC binding was detected as an increase in the fluorescence anisotropy of SRP(C421)-F5M. SRP binds tightly to the two cargos with the strongest signal sequences (RNC_{1A9L} and RNC_{2A8L}), with equilibrium dissociation constants (K_d) of ~1 nM or less (figure 5.1C and 5.S1). These values are similar to that for an SRP model substrate, RNC bearing the FtsQ signal sequence (figure 5.S1A); thus the behavior of authentic SRP substrates can be recapitulated by the engineered signal sequences. The next strongest

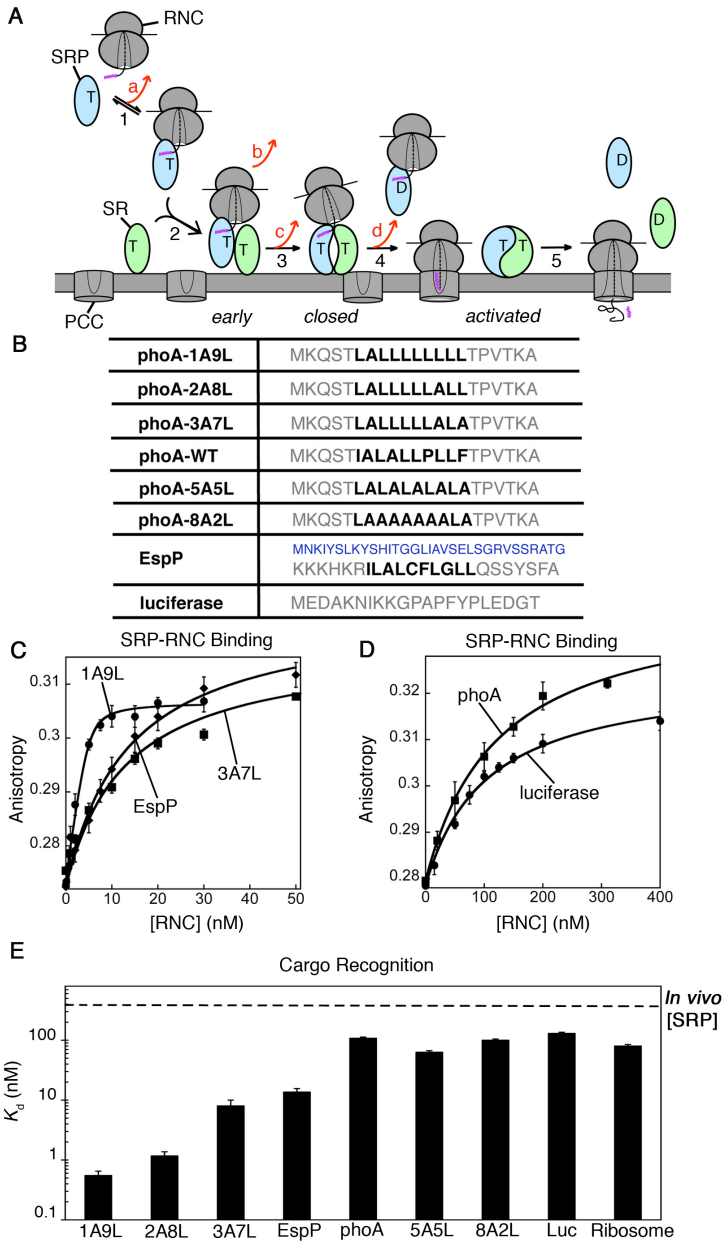

Figure 5.1. Potential fidelity checkpoints in the SRP pathway. (A) Model for potential checkpoints during co-translational protein targeting. A cargo bearing a signal sequence (magenta) enters this pathway upon binding the SRP, and is either retained (black arrows) or rejected (red arrows) at each checkpoint. T and D denote for GTP and GDP, respectively. (B) Signal sequence variants used in this study. Bold highlights the hydrophobic core. Blue denotes the unique N-terminal signal peptide extension in EspP. (C, D) Equilibrium titrations of SRP-RNC binding. Nonlinear fits of data gave K_d values of 0.55, 8.4, 13.6, 108 and 130 nM for RNC_{1A9L} (C, ●), RNC_{3A7L} (C, ■), RNC_{EspP} (C, ◆), RNC_{phoA} (D, ■) and $RNC_{luciferase}$ (D, ●), respectively. (E) Summary of the binding affinities of SRP for different cargos. The dashed line represents the cellular SRP concentration of ~400 nM.

cargo, RNC_{3A7L}, also exhibits strong albeit attenuated binding to SRP, with K_d ~ 10 nM (figure 5.1C). Cargos with even weaker signal sequences bind the SRP another 10 fold weaker (figure 5.1, D-E, and figure 5.S1). Nevertheless, the affinity of incorrect cargos or the empty ribosome for SRP is still substantial, with K_d's of 80 – 100 nM. In comparison, signal peptides bind SRP with K_d's in the micromolar range (*35, 106*). Thus interactions with the ribosome are important for recruiting the SRP to the cargo (*82, 85, 91, 107*). As the cellular SRP concentration is ~400 nM (*83*), at least four fold higher than the K_d values of SRP for even the weakest cargos (figure 5.1E, dashed line), a substantial amount of incorrect cargos could be bound at this SRP concentration. To our surprise, although EspP is not an SRP substrate, RNC_{EspP} binds SRP as tightly as RNC_{3A7L} (figure 5.1C). Thus the differences in cargo binding affinity may not provide sufficient discrimination against incorrect cargos, and additional factors in the bacterial cytosol do not increase the specificity of SRP-cargo binding (figure 5.S2) (*108*).

Besides SRP, the PCC also discriminates against incorrect cargos (*109, 110*). Nevertheless, the PCC mediates translocation of proteins from both the SRP- and SecB-pathways, including EspP (*111*), and hence is unlikely to be solely responsible for the stringent substrate selection by the SRP. We postulated that incorrect cargos could be less efficient during subsequent steps of targeting; these steps thereby provide additional checkpoints to help reject incorrect cargos (*112*). We tested several potential checkpoints: (i) Formation of the *early* SRP•SR complex (figure 5.1A, step 2), an obligatory intermediate preceding the formation of subsequent complexes (*4, 5*). This intermediate is highly unstable with free SRP, and >98% of it dissociates before rearranging into the subsequent complex. A strong cargo stabilizes the *early* intermediate and prevents its

premature disassembly (*5*). If incorrect cargos could not provide such a stabilization, then their *early* targeting complexes would be more likely to disassemble and exit the SRP pathway prematurely (figure 5.1A, arrow b). (ii) Rearrangement of the *early* intermediate to the *closed* complex (figure 5.1A, step 3), which is essential for switching the SRP from a cargo-binding to a cargo-releasing mode and primes the cargo for unloading (*5*). If incorrect cargos were less efficient in this rearrangement, then their late stages of targeting would be delayed (figure 5.1A, arrow c). (iii) GTP hydrolysis from the SRP•SR complex, which occurs rapidly in the absence of cargo (*66*). A strong cargo could delay GTP hydrolysis, providing the cargo•SRP•SR complex an important time window to search for the target membrane and the PCC before GTP hydrolysis drives the irreversible disassembly of the targeting complex (figure 5.1A, steps 4 vs. 5) (*5*). If incorrect cargos could not delay GTP hydrolysis as effectively, they would be more likely to be rejected through premature GTP hydrolysis (figure 5.1A, arrow d). This would further improve the fidelity of targeting via kinetic proofreading.

To test whether the *early* SRP•SR complex is stabilized more strongly by the correct than the incorrect cargo, we assembled cargo•SRP•SR *early* complexes in the absence of nucleotides; this blocks the rearrangement of the GTPase complex to subsequent conformations and allows us to isolate this intermediate (*4, 5*). The equilibrium stabilities of the *early* complexes were measured using fluorescence resonance energy transfer (FRET) between donor- and acceptor-labeled SRP and SR (*4*). In this and all the following experiments, saturating RNCs were used to ensure that 80 – 99% of the SRPs are loaded with cargo, such that differences in cargo binding affinities are bypassed. The *early* complex is significantly stabilized by RNC_{1A9L} and RNC_{2A8L},

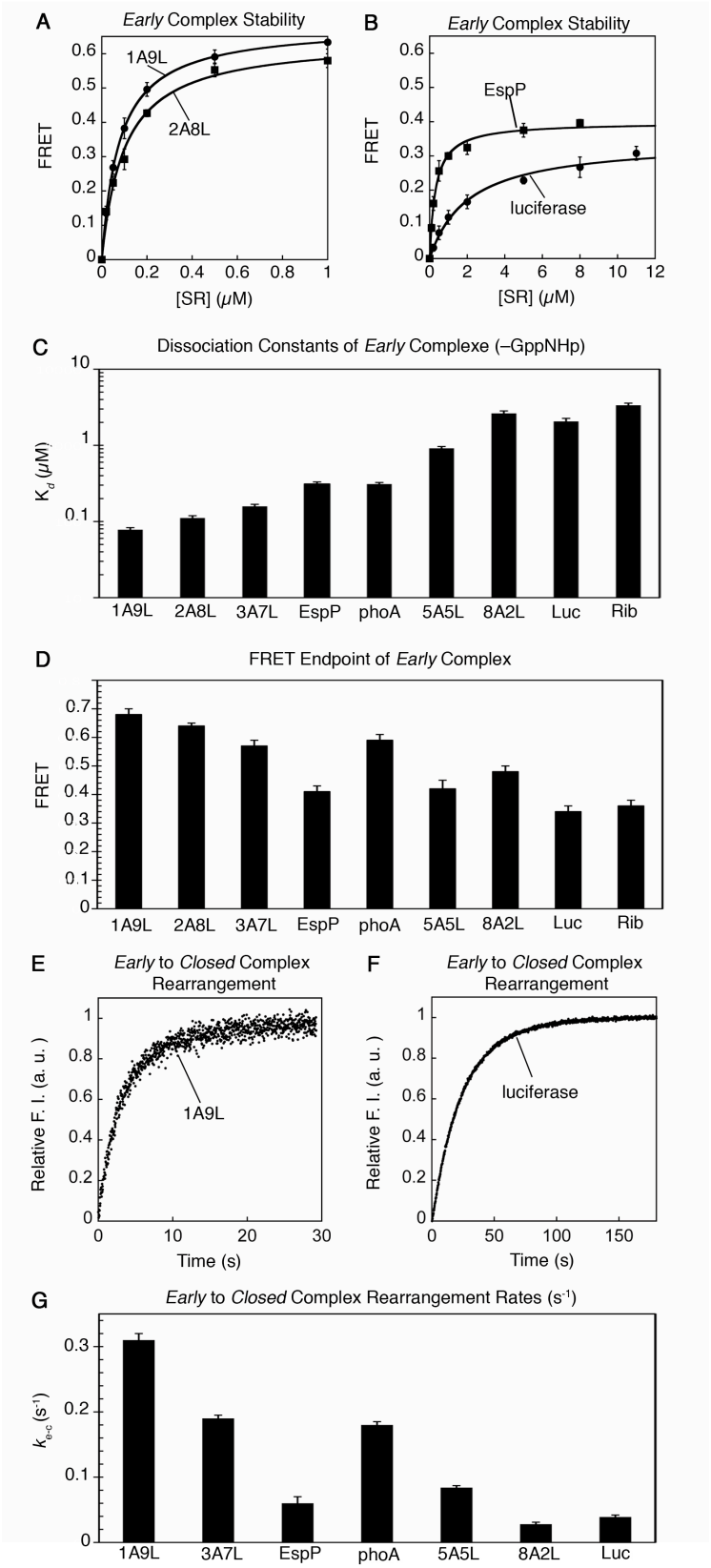
A
Early Complex Stability
1A9L
2A8L
FRET
[SR] (μM)
B
Early Complex Stability
EspP
luciferase
FRET
[SR] (μM)
C
Dissociation Constants of Early Complexe (–GppNHp)
K_d (μM)
1A9L 2A8L 3A7L EspP phoA 5A5L 8A2L Luc Rib
D
FRET Endpoint of Early Complex
FRET
1A9L 2A8L 3A7L EspP phoA 5A5L 8A2L Luc Rib
E
Early to Closed Complex Rearrangement
1A9L
Relative F. I. (a. u.)
Time (s)
F
Early to Closed Complex Rearrangement
luciferase
Relative F. I. (a. u.)
Time (s)
G
Early to Closed Complex Rearrangement Rates (s-1)
k_e-c (s-1)
1A9L 3A7L EspP phoA 5A5L 8A2L Luc

Figure 5.2. Correct cargos stabilize the *early* intermediate and mediate faster rearrangement to the *closed* complex. (A, B) Equilibrium titrations of the *early* intermediate. Nonlinear fits of data gave K_d values of 78, 110, 311 and 2060 nM and FRET endpoints of 0.68, 0.64, 0.41, and 0.34 for RNC_{1A9L} (A, ●), RNC_{2A8L} (A, ■), RNC_{EspP} (B, ■), and $RNC_{luciferase}$ (B, ●), respectively. (C, D) Summary of the K_d values (C) and FRET end points (D) of the *early* intermediates formed by different cargos. (E, F) Measurements of the *early* → *closed* rearrangement. Nonlinear fits of data gave rate constants of 0.31 s^{-1} with RNC_{1A9L} (E) and 0.039 s^{-1} with $RNC_{luciferase}$ (F). (G) Summary of the rate constants for the *early* → *closed* rearrangement with different cargos.

with K_d ~ 80 nM (figure 5.2A), and this stability is severely compromised for the weaker cargos (figure 5.2, B-C, and figure 5.S3). Further, with incorrect cargos such as RNC_{EspP} and $RNC_{luciferase}$, the FRET efficiency plateaus at a lower value, ~0.3 – 0.4 (figure 5.2, B and D, and figure 5.S3), compared to ~0.66 with the correct cargos (figure 5.2, A and D). This and the slower rate at which these *early* complexes rearrange to the *closed* state (see below) suggest that the SRP and SR are likely mispositioned in the *early* targeting complexes formed by the incorrect cargos. Thus weak or incorrect cargos do not induce the formation of a stable and productive *early* complex, and are more likely to exit the pathway prematurely (figure 5.1A, arrow b).

To test whether the rearrangement to the *closed* complex is more efficient with the correct than the incorrect cargos (figure 5.1A, step 3), we used acrylodan-labeled SRP(C235), which specifically detects formation of the *closed* complex (*5*). We preformed the *early* targeting complex in the absence of nucleotides and in the presence of saturating cargo and SR, and monitored its rearrangement into the *closed* complex upon addition of the GTP analogue 5'-guanylylimido-diphosphate (GMPPNP). With RNC_{1A9L}, this rearrangement is fast, occurring at 0.3 s^{-1} (figure 5.2E). RNC_{3A7L} and RNC_{phoA} mediated this rearrangement 40% slower (figure 5.2G and 5.S4). Notably, RNC_{EspP} and cargos weaker than RNC_{5A5L} mediate this rearrangement 5–10 fold slower

than RNC_{1A9L} (figure 5.2, F-G, and figure 5.S4). The slower rate of the *early* → *closed* rearrangement observed with these cargos correlated with their lower FRET value in the *early* intermediate (figure 5.2D), suggesting that efficient rearrangement to the *closed* complex requires formation of an *early* intermediate in a productive conformation.

The more favorable pre-equilibrium to form the *early* intermediate combined with the faster *early* → *closed* rearrangement would allow the correct cargos to mediate GTP-dependent SRP-SR complex assembly at much faster rates (figure 5.1A, steps 2-3). We characterized this cumulative effect using both FRET (figure 5.3, A-C, and figure 5.S5, F-G) and acrylodan-labeled SRP(C235) (figure 5.S5). Both probes demonstrated that the correct cargos mediate rapid SRP-SR complex assembly with GMPPNP (figure 5.3A and 5.S5A), and this rate decreases significantly as the signal sequence becomes weaker (figure 5.3B-C, and figure 5.S5). Both assays revealed a ~10^3 fold discrimination between the strongest (e.g., RNC_{1A9L}) and weakest (e.g., RNC_{EspP} & RNC_{8A2L}) cargos in the kinetics of GTP-dependent complex assembly (figure 5.3C and 5.S5E). This is consistent with the cumulative effect of the over 50 fold more stable *early* intermediate (figure 5.2C) and the ~10 fold faster rate at which this intermediate rearranges to the *closed* complex (figure 5.2G) with the correct than the incorrect cargos.

To test whether the correct cargos delay GTP hydrolysis more effectively than the incorrect cargos, we determined the rate of the GTPase reaction from the cargo•SRP•SR complexes. RNC_{1A9L} and RNC_{2A8L} reproducibly delay GTP hydrolysis 6–8 fold (figure 5.3D and 5.S6). The next strongest cargo, RNC_{3A7L}, has a smaller but still substantial inhibitory effect on the GTPase reaction (figure 5.S6). In contrast, incorrect cargos such as RNC_{EspP} inhibit GTP hydrolysis by less than two fold, and $RNC_{luciferase}$ does not

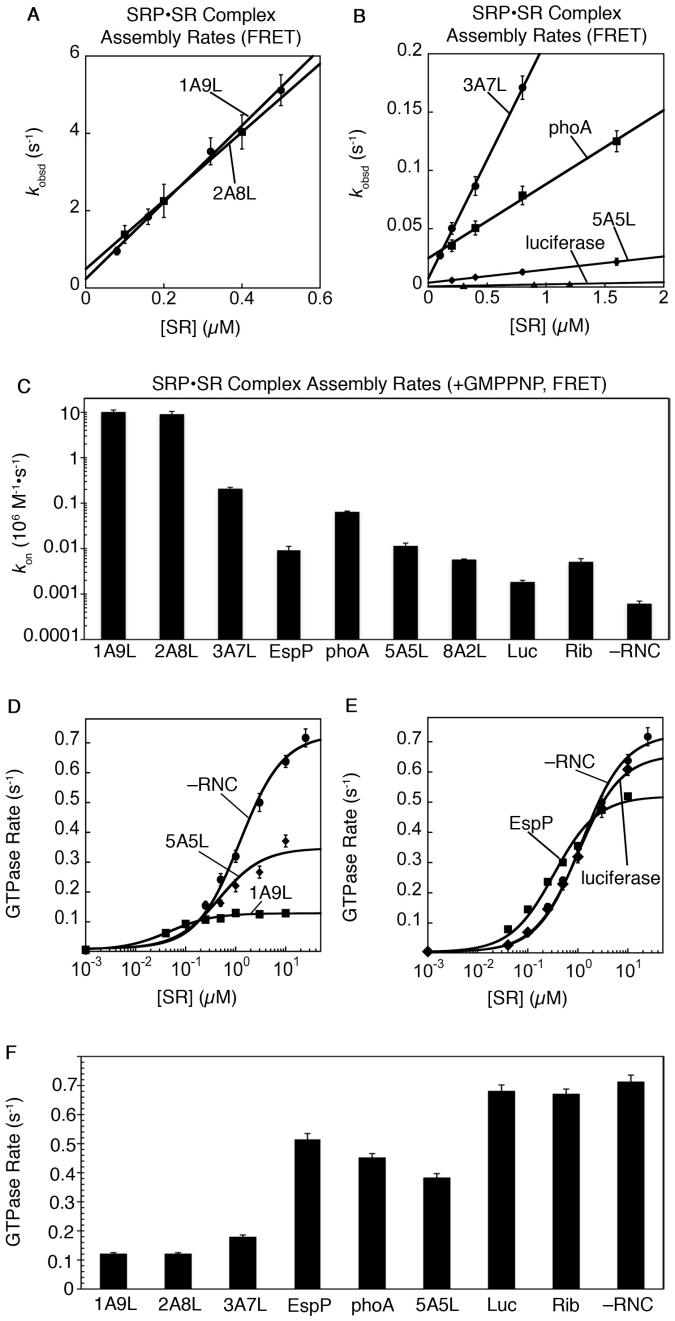

Figure 5.3. Correct cargos accelerate GTP-dependent complex formation but delay GTP hydrolysis. (A, B) Rate constants of SRP-SR complex assembly in GMPPNP measured by FRET. k_{on} values of 9.9×10^6, 8.8×10^6, 2.0×10^5, 2.2×10^4, 1.1×10^4 and 1.8×10^3 $M^{-1}s^{-1}$ for RNC_{1A9L} (A, ●), RNC_{2A8L} (A, ■), RNC_{3A7L} (B, ●), RNC_{phoA} (B, ■), RNC_{5A5L} (B, ◆) and $RNC_{luciferase}$ (B, ▲), respectively. (C) Summary of GTP-dependent complex assembly rate constants with different cargos. (D, E) Effects of cargo on GTP hydrolysis from the SRP•SR complex. k_{cat} are 0.72 s^{-1} without cargo (●), and 0.11, 0.34, 0.51, and 0.65 s^{-1} with RNC_{1A9L} (D, ■), RNC_{5A5L} (D, ◆), RNC_{EspP} (E, ■) and $RNC_{luciferase}$ (E, ◆), respectively. (F) Summary of GTPase rate constants in the presence of different cargos.

significantly affect the GTPase rate (figure 5.3, E-F, and figure 5.S6). These results are consistent with the hypothesis that the fidelity of protein targeting can be further improved through kinetic proofreading mechanisms by using the energy of GTP hydrolysis (figure 5.1A, arrow d).

These results demonstrate that the SRP pathway discriminates against incorrect cargos not only through binding affinity, but also through differences in the kinetics of SRP-SR complex assembly and GTP hydrolysis. Another important determinant of co-translational protein targeting is the length of the nascent polypeptide, as the SRP loses its ability to target substrates when the nascent chain exceeds ~110 residues (*87, 113*). Since the bacterial SRP does not arrest translation (*2*), this gives a ~3 second time window for the SRP to complete protein targeting (*112*), assuming that SRP begins to recognize cargos when the nascent chain is ~35 amino acids long and a translation elongation rate of ~20–30 amino acids/second in bacteria *(114)*. Based on this time constraint and the rate and equilibrium constants determined here, we calculated the amount of substrates retained in the SRP pathway after each checkpoint (figure 5.4A). The cargo binding step is not sufficient to discriminate against incorrect cargos, allowing over 75% of them to enter the SRP pathway (figure 5.4A, light grey). During cargo delivery through GTP-dependent SRP-SR complex assembly, a large portion of substrates weaker than phoA are rejected (figure 5.4A, dark grey). Finally, kinetic competition between GTP hydrolysis and cargo unloading allows most of the incorrect substrates to be rejected, whereas the majority of substrates stronger than phoA-3A7L are retained (figure 5.4A, black).

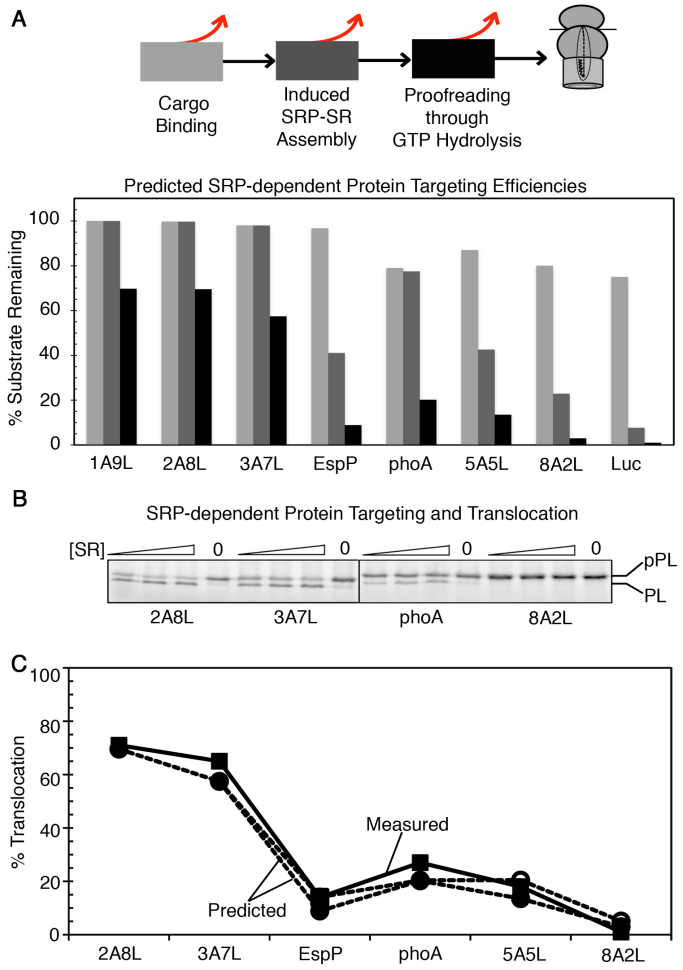

Figure 5.4. Stepwise rejection of weak or wrong cargos from the SRP pathway. (A) The fraction of cargos remaining in the SRP pathway after each step, calculated as described in the Methods. As depicted in the top panel, cargos are either retained (black arrow) or rejected (red arrow) from the pathway during cargo binding (light grey), induced SRP-SR assembly (dark grey), and proofreading through GTP hydrolysis (black). (B) SRP-dependent protein targeting and translocation of substrates with different signal sequences analyzed by SDS-PAGE. pPL and PL denote the precursor and signal sequence-cleaved forms of the substrate, respectively. (C) Predicted protein targeting efficiencies (● and ○) agree well with the experimentally determined values (■), quantitated from the data in (B). Translation elongation rates of 20 (●) and 10 amino acids/s (○) were used for the *E. coli* and eukaryotic ribosomes, respectively, to calculate the targeting efficiencies. The small discrepancies between the measured and calculated targeting efficiencies based on *E. coli* ribosomes could be rationalized by a slower translation rate of eukaryotic ribosome used in the assay than that of *E. coli* ribosome used in the calculations (*115*), which gives the SRP and SR a longer time window for complex assembly. This discrepancy became smaller when the calculation was performed using the translation rate of eukaryotic ribosomes (○).

To test the validity of this analysis, we determined the targeting efficiency of proteins with various signal sequences using a well-established assay that tests the ability of *E. coli* SRP and SR to mediate the co-translational targeting of preproteins to microsomal membranes (*44, 116*). Cleavage of preprolactin (pPL) signal sequence provides readout for successful targeting and translocation (figure 5.4B). Bacterial SRP and SR mediate pPL targeting as efficiently as their mammalian homologues despite the heterologous nature of this assay (*44*); this highlights the remarkable conservation of the SRP pathway and allows us to test insights from biophysical studies of bacterial SRP and SR in the context of a complete and functional targeting reaction. Importantly, as both reaction substrates and products are quantitated, this assay provides the most accurate measure of targeting efficiency. Substrates with signal sequences stronger than 3A7L are efficiently targeted and translocated (figure 5.4B and 5.S7). In contrast, substrates with the EspP signal sequence or signal sequences weaker than phoA show severe defects in translocation, and almost no translocation was detected for the phoA-8A2L substrate (figure 5.4B). Remarkably, the experimentally determined protein targeting efficiencies agree well with predictions based on the kinetic and thermodynamic measurements (figure 5.4C), suggesting that our model (figure 5.1A) faithfully represents the way SRP handles its substrates.

5.4 Discussion

Our work supports a novel model in which fidelity is achieved during co-translational protein targeting through the cumulative effect of multiple checkpoints, by using a combination of binding, induced fit, and kinetic proofreading mechanisms. With

correct substrates, loading of cargo is coupled to its rapid delivery (through accelerated complex assembly) and productive unloading (through delayed GTP hydrolysis); whereas with incorrect cargos stable SRP-SR complex assembly is extremely slow, but once the stable complex is formed rapid GTP hydrolysis immediately drives its disassembly. These differences in downstream steps strongly suggest that incorrect cargos bind the SRP in a less productive mode than the correct cargos (*92*). The lack of productive interactions with the signal sequence did not lead to complete rejection of incorrect cargos during the initial binding step, but were detected during subsequent steps and discriminated repeatedly. This conclusion is most strongly supported by the case of EspP, which binds SRP strongly but is rejected primarily by kinetic discrimination in the complex assembly and GTP hydrolysis steps. Our analyses here focused on how the SRP handles each substrate in a single round of targeting. *In vivo,* a higher fidelity could be achieved during multiple rounds of targeting and with competition between correct and incorrect cargos. In addition, the PCC provides another important checkpoint to discriminate against incorrect cargos such as phoA-8A2L (*109, 110*); we could not detect this additional discrimination as the targeting efficiency of this substrate before arrival at PCC is already ≤1%.

Our findings are analogous to those observed in tRNA selection during translation, in which a mismatch between the mRNA and tRNA anticodon at the ribosome active site leads not only to weaker binding affinities for the noncognate and near-cognate tRNAs, but also to slower rates of subsequent steps and higher frequency of rejection of the non- and near-cognate tRNAs (*117, 118*). Similar strategies of using multiple checkpoints to ensure fidelity have been demonstrated by pioneering work on

tRNA synthetases (*119*) and DNA and RNA polymerases (*120, 121*), and likely represents a general principle for complex cellular pathways, especially those that need to recognize degenerate signals or to discriminate between substrates based on minor differences.

5.5 Materials and Methods

5.5.1 Materials

The *E. coli* SRP and SR GTPases (Ffh and FtsY, respectively), trigger factor, and 4.5S RNA were expressed and purified as described previously (*66, 122*). FtsY(47-497) was used in all the fluorescence measurements, and full length FtsY was used in GTPase rate measurements. The abilities of FtsY(47-497) to interact with SRP and respond to the cargo are similar to those of full length FtsY (*5*). Single cysteine mutants of Ffh and FtsY were constructed using the QuickChange mutagenesis procedure (Stratagene), and were expressed and purified using the same procedure as that for the wild-type proteins. Fluorescent dyes N-(7-dimethylamino-4-methylcoumarin-3-yl)maleimide (DACM), fluorescein-5-maleimide (F5M), and BODIPY-FL-N-(2-aminoethyl)-maleimide were from Invitrogen.

5.5.2 Signal sequence mutants

Plasmids encoding signal sequence variants were constructed based on pUC19StrepFtsQSecM (*67*), composed of a strep3 tag in the N terminus, the first 74 amino acids of FtsQ, and a translation stall sequence from SecM (residues 136-166). For this work, FtsQ (1-74) was replaced with the first 50 residues of phoA or firefly luciferase, and mutations were introduced into the hydrophobic core of phoA (figure 1B in main text) using the QuickChange mutagenesis procedure (Stratagene).

5.5.3 RNC and ribosome purification

70S ribosomes were purified from *E coli* MRE600 cells following established

protocols (*5, 95*). Homogeneous RNCs were generated from *in vitro* translation reactions using membrane free cell extract prepared from MRE600 cells, and purified through affinity chromatography and sucrose gradient centrifugation as described previously (*5, 95*). RNCs purified using this method can bind SRP, TF, and the secYEG complex (*67*) and in quantitative assays, exhibit the same affinity for SRP as those measured with RNCs that do not contain an affinity tag (*68*).

5.5.4 SRP- and ribosome-free *E. coli* (*-ffh*) total cytoplasmic extract

The bacterial strain HDB51 MC4100 *ara+ secB+ zic-4901*::Tn*10 ffh*::*kan-1* λ(Para-*ffh* Apr), in which the expression of Ffh is under the control of arabinose promoter, was a generous gift from Harris D. Bernstein at NIDDK, NIH (*123*). Bacterial culture was grown at 37 ºC in the absence of arabinose for 4-5 generations so that more than 90% of endogenous Ffh was depleted (*123*). Cells were harvested at $OD_{600} = 0.70$. The cell pellet was washed with 0.1M Tris•HCl buffer (pH 8.0), and resuspended in lysis buffer [0.1M Tris•HCl, 20% sucrose, 1mM phenylmethylsulphonyl fluoride (PMSF), and 50 μg/mL lysozyme] for 90 minutes at room temperature. $MgCl_2$ was then added to stabilize the spheroplasts at a final concentration of 20 mM. The mix was spun at 8000 rpm for 10 min to separate spheroplasts from the periplasmic fraction. The spheroplasts were washed twice in buffer containing 0.1M Tris•HCl (pH 8.0), 20% sucrose, and 20 mM $MgCl_2$, resuspended in PBS containing 1mM PMSF, and passed through French Press three times at 10,000 psi. The lysate was clarified by centrifugation at 8000 rpm for 10 minutes, and ultracentrifuged twice at 320,000 g for 3 hours at 4ºC to remove membranes and ribosomes. The supernatant was collected as the cytosolic extract.

5.5.5 Fluorescence labeling

For FRET measurements, DACM and BODIPY-FL were used to label single-cysteine mutants of Ffh and FtsY, respectively, as described previously (*4*). For measurements using environmental sensitive probes, acrylodan was used to label Ffh(C235) as described (*5*). For fluorescence anisotropy measurements, F5M was used to label Ffh(C421). Fluorescence labeling with F5M followed the same procedure as those for DACM and BODIPY-FL. Labeled protein was purified as described (*4*), and the concentration of labeled protein was determined using an absorption extinction coefficient of $\varepsilon_{504} = 83{,}000\ M^{-1}\ cm^{-1}$ for F5M. The efficiency of labeling was typically ≥95% with a background of <5%.

5.5.6 Fluorescence anisotropy measurements

Anisotropy measurements used an excitation wavelength of 450 nm and emission wavelength of 518 nm. Fluorescence anisotropy was calculated according to Eq. 5.1:

$$R = \frac{\left(I_{VV} - G \times I_{VH}\right)}{\left(I_{VV} + 2G \times I_{VH}\right)} \tag{5.1}$$

in which I_{VV} and I_{VH} are the vertically and horizontally polarized emission intensities when the sample is vertically excited, G is the grating factor that corrects for the wavelength response to polarization of the emission optics and detectors, defined as $G = I_{HV}/I_{HH}$, where I_{HV} and I_{HH} are the vertically and horizontally polarized emission intensities when the sample is horizontally excited.

5.5.7 Fluorescence measurements

All measurements were carried out at 25 °C in assay buffer [50 mM KHEPES, pH 7.5, 150 mM KOAc, 10 mM $Mg(OAc)_2$, 2 mM DTT] on a Fluorolog-3-22 spectrofluorometer (Jobin Yvon, Edison, NJ). The detergent Nikkol, which was used in previous work, was not used for studies of complex assembly in this work. The stimulatory effects of strong SRP cargos can be observed without removing Nikkol (*4*), and the same SRP-SR complex assembly rate constants and stability of the *early* complex was observed with the strong cargos (RNC_{1A9L}, RNC_{2A8L}, and RNC_{3A7L}) with or without Nikkol present. On the other hand, Nikkol obscures the small stimulatory effects from weak cargos or the empty ribosome, as the complex assembly rate constant between free SRP and SR is ~100 fold faster in the presence of Nikkol (*106*).

FRET measurements were carried out using an excitation wavelength of 380 nm and an emission wavelength of 470 nm. FRET efficiency was calculated as described (*4*). For measurements using acrylodan-labeled SRP(C235), an excitation wavelength of 380 nm was used and fluorescence emission at 500 nm was monitored (*5*).

5.5.8 Strategy to isolate individual reaction steps during protein targeting

This section describes how the individual reaction rate or equilibrium constants were isolated using the principles of rate laws, rate-limiting steps, the rules of thermodynamics and mass action, and the information acquired for a previous reaction step. In general, each time a subsequent reaction step was measured, reaction conditions were designed such that all the cargos have passed the previous steps.

5.5.8.1 ***Cargo binding to the SRP (figure 1A, step 1)***

The equilibrium binding affinity of SRP for various cargos was determined by equilibrium titration using the change in the fluorescence anisotropy of F5M-labeled SRP(C421). In general, 5 – 20 nM SRP and 100 μM GMPPNP were used in the titrations. We found that cargos bind to and dissociate from the SRP on a time scale faster than manual mixing (30 sec – 1 min). Therefore, all samples were incubated for 2 – 5 minutes to ensure that equilibrium has been established. In each measurement, increasing amounts of cargo were added to a fixed amount of fluorescently labeled SRP. The anisotropy value (A) at different SRP concentrations were plotted as a function of cargo concentration ([RNC]). The data were fit to single binding (Eq. 5.2) or quadratic (Eq. 5.3) equations,

$$A = A_0 + (A_1 - A_0) \times \frac{[RNC]}{K_d + [RNC]} \tag{5.2}$$

$$A = A_0 + (A_1 - A_0)\left\{\frac{c_0 + [\mathrm{RNC}] + K_d - \sqrt{(c_0 + [\mathrm{RNC}] + K_d)^2 - 4c_0[\mathrm{RNC}]}}{2c_0}\right\} \tag{5.3}$$

in which A_0 is the anisotropy value of free SRP, A_1 is the anisotropy value when SRP is bound to cargo, c_0 is the concentration of total SRP, and K_d is the equilibrium dissociation constant of SRP for the RNC. No significant changes were found in fluorescence intensity of free- and bound-SRP after photo-bleaching effect was corrected.

5.5.8.2 ***Formation of the SRP•SR early intermediate (figure 1A, step 2)***

During the measurement of this and all subsequent steps, all reactions were carried out in the presence of saturating cargo concentrations (100 nM RNC_{1A9L} and

RNC_{2A8L}, 200 nM RNC_{3A7L} and RNC_{EspP}, 500 nM RNC_{phoA}, RNC_{5A5L} and RNC_{8A2L}, 600 nM $RNC_{luciferase}$, and 1 μM ribosome). This ensures that 80–99% of the SRP are bound to the cargos so that the differences in cargo binding affinities contribute less than 20% to our measurements.

Our previous work showed that the rate constant of *early* complex formation is rapid and affected only two fold by a strong cargo, and that the primary effect of cargo is on the stability of the *early* complex. We therefore measured the equilibrium stability of the *early* complex formed by different cargos using the FRET assay. Equilibrium titrations were carried out in the presence of a small, fixed amount of RNC-bound, donorlabeled SRP and increasing amounts of acceptor-labeled SR in the absence of GTP or GTP analogues. Equilibrium was established upon manual mixing. FRET efficiency was calculated as described and plotted as a function of SR concentration ([SR]). The data were fit to Eq. 5.4,

$$E = E_1 \times \frac{[SR]}{K_d + [SR]} \tag{5.4}$$

in which E_1 is the FRET value (end point) when all the cargo•SRP complexes are bound to SR, and K_d is the equilibrium dissociation constant of the *early* intermediate.

The early → closed rearrangement (figure 1A, step 3). This rearrangement was measured using acrylodan-labeled SRP(C235), which specifically detects the *closed* complex (*5*). The *early* cargo•SRP•SR complexes were pre-assembled in the presence of 0.1 – 0.25 μM acrylodan-labeled SRP(C235), saturating cargo and SR with respect to their K_d values, and in the absence of nucleotides. An excess of GMPPNP (400 μM) was added to initiate the rearrangement to the *closed* complex and the fluorescence intensity of

acrylodan (*I*) was monitored over time. The time courses were single exponential and fit to eq 5.5,

$$I(t) = I_1 + (I_0 - I_1) \times \exp(-k_{obsd} t) \quad (5.5)$$

in which I_0 is the fluorescence before addition of GMPPNP, I_1 is the fluorescence value at $t \rightarrow \infty$, and k_{obsd} is the observed rate constant. In all cases, we ensured that SR concentrations were sufficiently high such that the values of k_{obsd} were independent of SR concentration, confirming that the unimolecular rearrangement within the GTPase complex was isolated. With free SRP, this method gives the same rate constant for this rearrangement (1.5 s^{-1}) as that previously measured during a continuous FRET assay in which the *early* complex was not first stalled by leaving out GTP (1-2 s^{-1}) *(4)*. Further, when acrylodan-labeled SRP(C235) was used to monitor SRP-SR complex assembly with RNC_{1A9L}, at high SR concentrations the observed assembly rate constant deviated from linearity and plateaued, indicating that the reaction was rate limited by the early to closed rearrangement at saturating SR concentrations. The rate of the rearrangement obtained from this plateau was 0.34 s^{-1} (figure 5.S9), comparable to that of 0.31 s^{-1} measured using the pulse-chase experiment (figure 5.2E and G in main text). Together, the remarkable agreement between the different methods indicates that: (i) the *early* intermediate isolated in the absence of nucleotides is kinetically competent for subsequent rearrangements; and (ii) our approach of isolating the *early* intermediate and chasing it to the *closed* complex provides a valid method to measure the rate of this conformational rearrangement.

Rate constants for GTP-dependent SRP-SR complex assembly (figure 1A, steps 2+3). The

second-order rate constant for SRP-SR association to form the GTP-stabilized *closed* complex was measured using acrylodan-labeled SRP(C235). A constant concentration of cargo-bound, labeled SRP was mixed with varying concentrations of SR to initiate complex assembly, and the changes in the fluorescence of acrylodan-labeled SRP(C235) was monitored over time. The data were fit to Eq. 5.5 above to obtain the observed rate constants (k_{obsd}) at individual SR concentrations. The values of k_{obsd} were plotted as a function of SR concentrations of SR ([SR]) and fit to Eq. 5.6,

$$k_{obsd} = k_{on} \bullet [SR] + k_{off} \tag{5.6}$$

in which k_{on} and k_{off} are the rate constants for complex assembly and disassembly, respectively. Fast reactions were measured on a Kintek stopped-flow apparatus. As an independent way to measure the second order rate constant for stable SRP-SR complex assembly, FRET instead of the environmentally sensitive probes was used and the rate constants were determined analogously. The conditions for measuring complex assembly rate constants are: 100 μM GMPPNP; 80 nM SRP and 100 nM RNC_{1A9L} or RNC_{2A8L}; 100 nM SRP and 200 nM RNC_{3A7L} or RNC_{EspP}; 200 nM SRP and 500 nM RNC_{phoA}, RNC_{5A5L} or RNC_{8A2L}, 300 nM SRP and 600 nM $RNC_{luciferase}$.

These two methods provide independent and complementary information about the rate constants of complex assembly. Acrylodan-labeled SRP(C235) allows us to specifically measure the assembly rate of the *closed* complex. FRET, on the other hand, reports on the formation of a stable targeting complex that includes both the *early* and *closed* conformational states. For most of the cargos, these two methods yield the same rate constants within experimental error (cf. figure 5.3C vs figure 5.S5E). For RNC_{1A9L} and RNC_{2A8L}, the rate constants measured by FRET is ~10 fold faster than by

acrylodanlabeled SRP(C235). This is because with these two cargos, the *early* intermediate is similar in stability to the *closed* complex; hence the SRP•SR complex formed by these cargos in GMPPNP is a roughly equal mixture of the *early* and *closed* states, both of which are detected by FRET but only the latter was detected by acrylodan-labeled SRP(C235). Because stable complex formation bypasses the *early* → *closed* rearrangement with these two cargos, their rate constant for GTP-dependent complex assembly detected by FRET is faster than that detected by acrylodan-labeled SRP(C235). In contrast, for cargos weaker than RNC_{3A7L}, the *closed* complex is the predominant conformation and its formation was monitored by both probes. Because complex assembly is rapid and not rate-limiting for the GTPase cycles and for protein targeting with RNC_{1A9L} and RNC_{2A8L}, roughly the same results (with differences of <2%) were obtained in numerical analysis of their protein targeting efficiencies regardless of whether the complex assembly rate constants measured by the FRET or acrylodan probes were used for the calculation.

GTP hydrolysis from the SRP•SR complex (figure 1A, step 4). The GTPase assay to measure the stimulated GTP hydrolysis reaction between SRP and FtsY was carried out and analyzed as described (*66*). 40 – 50 nM SRP were loaded with cargo in the presence of increasing SR concentrations, and the reactions were initiated by addition of 100 μM GTP doped with γ-^{32}P-GTP. The SR concentration dependence of the observed GTPase rate constant (k_{obsd}) was fit to eq. 5.7,

$$k_{obsd} = k_{cat} \times \frac{[SR]}{[SR] + K_m} \tag{5.7}$$

in which k_{cat} is the rate constant at saturating SR concentration, and K_m is the SR

concentration required to reach half saturation. It should be noted that in this assay, the observed rate constants at subsaturating SR concentrations represents the second order reaction: ^{GTP}•SRP + SR•^{GTP} → 2GDP + 2P_i, and is rate-limited by complex assembly between the SRP and SR. The rate constant observed at saturating SR concentrations (k_{cat}) represents the GTPase rate constant from a fully formed, stable cargo•SRP•SR complex, and is the parameter relevant in this study. Nikkol was included in the GTPase assay as the rate of GTP hydrolysis from the SRP•FtsY complex was not affected by Nikkol (*106*), and inclusion of Nikkol allows saturation to be achieved at much lower FtsY concentrations.

5.5.9 Co-translational protein targeting and translocation

A previously established heterologous protein targeting assay (*44, 116*), based on the ability of *E. coli* SRP and FtsY to mediate the targeting of preprolactin (pPL) to microsomal membranes, was used in this study. Bacterial SRP and SR mediate pPL targeting as efficiently as their mammalian homologues despite the heterologous nature of this assay (*44*); this highlights the remarkable conservation of the SRP pathway and allows us to test insights from biophysical studies of bacterial SRP and SR in the context of a complete and functional targeting reaction. Importantly, as both substrates and products are quantitated, this assay provides the most accurate measure of targeting efficiency. Therefore, it is by far the most suitable assay for the purpose of this study.

ER microsomal membranes have been washed with EDTA, high salt, and digested with trypsin to remove the endogenous SRP and SR, as described previously (*44*). 200 nM SRP and 4 equiv. of washed and trypsin-digested microsomal membrane

were used in the targeting reaction. *E. coli* SRP binds to *E. coli* ribosomes with similar affinity (K_d = 80 nM) as those measured previously for the binding of SRP to wheat germ ribosomes (K_d = 71 nM) (*87*). Further, *E. coli* SRP and FtsY can mediate the targeting and translocation of preproteins as efficiently as mammalian SRP and SR despite the heterologous nature of this assay (*44*). This strongly suggests that the SRP-ribosome interactions are highly conserved across species and that the heterologous targeting assay provides a reasonable system to test insights from our biophysical measurements in the bacterial system in the context of a complete and functional targeting reaction. Constructs for the protein translocation assay were based on the plasmid pSPBP4. The hydrophobic core of the pPL signal sequence was replaced with the model signal sequences (figure 5.S7) using the QuickChange mutagenesis procedure (Stratagene).

5.5.10 Numerical analysis of protein targeting efficiency

This analysis estimates the fraction of each cargo that can be successfully targeted by the SRP pathway within a limited time window, t_w, before the nascent chain exceeds ~110 residues (*113*). This time window was based on the consideration that the SRP loses its ability to target substrates when the nascent chain exceeds ~110 residues (*87, 113*). Since the bacterial SRP does not arrest translation (*2*), this gives a t_w of ~3 second (or 6 second when eukaryotic ribosome was used) for the SRP to complete protein targeting (*112*), assuming that SRP begins to recognize cargos when the nascent chain is ~35 amino acids long and a translation elongation rate of ~20–30 amino acids/second in bacteria (or 10-15 amino acids/second for eukaryotic ribosome) *(114)*.

During the first step, the fraction of cargos that bind to SRP is calculated from:

$P(1) = [SRP]/(K_d + [SRP])$, using a cellular SRP concentration of 400 nM (*83*) and the K_d values from figure 5.1. During the second step, the fraction of cargos that are delivered to the membrane after stable SRP-SR complex assembly is calculated from: $P(2) = P(1) \times \exp(-k_{on}[SR] \times t_w)$, using a SR concentration of 2 μM (as was the condition used in the protein targeting reactions in figures 5.4B and 5.S7), the k_{on} values determined in Figure 5.3C, and a time window (t_w) of 3- or 6-seconds for *E coli* and eukaryotic ribosomes, respectively. During the last step, the fraction of cargos that can be unloaded to the protein conducting channel (PCC) before GTP hydrolysis is calculated from: $P(3) = P(2) \times \left[1 - \exp\left(-k_{GTPase} \times t_{PCC}\right)\right]$, using the GTP hydrolysis rate constants (k_{GTPase}) determined in Figure 5.3F. t_{PCC} denotes the lifetime for cargo unloading and was estimated to be ~3 s, as in the presence of the correct cargos the late conformational changes in the SRP•SR GTPase complex that are important for driving cargo unloading become rate limiting (*5*) and likely takes the majority of the 3s time window for protein targeting.

5.6 Supplementary text

5.6.1 A sequential model for rejection of incorrect cargos by additional checkpoints in the SRP pathway following the cargo-binding step

In this chapter, we postulated and tested the model that after the cargos are loaded on the SRP, the incorrect cargos could be less efficient during subsequent steps of targeting; these steps thereby provide additional checkpoints to help reject incorrect cargos (*35*). We considered the following potential checkpoints: (1) Formation of the *early* SRP•SR complex (figure 5.1A, step 2), an obligatory intermediate preceding the formation of subsequent complexes (*4, 5*). This intermediate is highly unstable with free SRP, and >98% of it dissociates before rearranging into the subsequent complex. A strong cargo could stabilize the *early* intermediate and prevent its premature disassembly (*5*). If incorrect cargos could not provide such a stabilization, then their *early* targeting complexes would be more likely to disassemble and exit the SRP pathway prematurely (figure 5.1A, arrow b). (2) Rearrangement of the *early* intermediate to the *closed* complex (figure 5.1A, step 3), which is essential for switching the SRP from a cargo-binding to a cargo-releasing mode and primes the cargo for unloading (*5*). If incorrect cargos were less efficient in this rearrangement, then their late stages of targeting would be delayed (figure 5.1A, arrow c). (3) GTP hydrolysis from the SRP•SR complex, which occurs rapidly in the absence of cargo (*66*). A strong cargo could delay GTP hydrolysis, providing the cargo•SRP•SR complex an important time window to search for the target membrane and the PCC before GTP hydrolysis drives the irreversible disassembly of the targeting complex (figure 5.1A, steps 4 *vs*. 5) (*5*). If incorrect cargos could not delay GTP hydrolysis as effectively, they would be more likely to be rejected through

premature GTP hydrolysis (figure 5.1A, arrow d). This would further improve the fidelity of targeting via kinetic proofreading. Beside SRP, the protein translocation machinery also discriminates against incorrect cargos (*109, 110*). However, the translocation machinery mediates translocation of proteins from both the SRP- and SecB-pathways, including EspP (*111*). Thus it is unlikely to be solely responsible for the stringent substrate selection by the SRP.

5.6.2 *E. coli* cytosolic factors do not compete with SRP for binding the RNC

It has been suggested that cellular chaperones that interact with translating ribosomes, such as trigger factor (TF), can compete with SRP for binding to the RNCs and thus increase the specificity of SRP-cargo binding (*107, 124*). However, the presence of up to 80 μM TF did not compete away the binding of SRP to either the correct (RNC_{ftsQ}), borderline (RNC_{phoA}), or incorrect ($RNC_{luciferase}$) cargos (figure S2A), consistent with previous findings (*108*). Even in the presence of SRP- and ribosome-free *E. coli* total cytosolic extract (see Methods), SRP-RNC binding affinities were not significantly affected (figure 5.S2, B-C). These results strongly suggest that cytosolic factors do not compete with SRP to increase the specificity of SRP-cargo binding.

5.6.3 Additional considerations of substrate selection by the SRP in vivo

The analyses in this work considered how the SRP handles each substrate protein during a single round of protein targeting. In vivo, a higher fidelity could be achieved by the SRP because of several factors. First, correct cargos are delivered more rapidly than the incorrect cargos; this would allow a larger number of the correct than incorrect cargos

to be targeted within a given time window during multiple rounds of protein targeting. Second, the SRP-SR interaction kinetics could be slower in vivo than in vitro, as protein diffusion rates tend to be slower within the crowded cellular environment. This would render the SRP-SR complex assembly step more rate-limiting for the targeting reaction in vivo and thus increase the contribution of this step to rejection of borderline substrates such as phoA. On the other hand, the membrane association of the SRP receptor FtsY could also affect the kinetics of SRP-SR interactions and the cargo unloading steps, rendering these downstream step(s) more or less rate-limiting. However, FtsY's localization could not affect the interaction of free SRP with the RNC, and thus would not change the conclusion that differences in SRP-cargo binding affinities do not provide sufficient discrimination against the incorrect cargos. Finally, competition between the strong and weak cargos may lower the effective concentration of free SRP in vivo; this would allow some of the discrimination in SRP's cargo binding affinities to be realized. Nevertheless, regardless of the effective SRP concentration in vivo, mechanisms based solely on discrimination in SRP-cargo binding affinities would not be able to reproduce the experimentally observed pattern of substrate selection (figure 5.S8). Under all conditions, such a mechanism predicts that EspP would be targeted with similar efficiency as phoA-3A7L, and that phoA, phoA-5A5L and phoA-8A2L would be targeted with the same efficiencies (figure 5.S8, dashed lines); these predictions are not supported by experimental data (figure 5.S8, red). Thus subsequent steps following cargo binding would be essential for the SRP to select the correct set of substrate proteins even in the presence of competition between correct and incorrect cargos. In addition, the secY translocation machinery provides another important checkpoint to discriminate against

incorrect cargos such as phoA-8A2L (*109, 110*); we could not detect this additional discrimination as the targeting efficiency of this substrate before arrival at the translocation machinery is already ≤1%.

5.6.4 Table

Table 5.S1. Kinetic and thermodynamic parameters for individual reaction step during SRP-dependent protein targeting in the presence of various cargos. Error bars are SDs from three independent experiments.

	K_d (nM) RNC binding	K_d (nM) early complex	FRET end point early complex	$k_{e\rightarrow c}$ (s^{-1}) early→closed rearrangement	k_{on} ($M^{-1}\bullet s^{-1}$) closed complex	GTPase rate (s^{-1})
1A9L	0.55 ± 0.20	78 ± 5	0.68 ± 0.02	0.31 ± 0.02	9.9 ± 1.3×10^6	0.11 ± 0.01
2A8L	1.2 ± 0.20	110 ± 8	0.64 ± 0.02	N.D.	8.8 ± 1.6×10^6	0.12 ± 0.02
3A7L	8.4 ± 2.0	158 ± 10	0.57 ± 0.02	0.19 ± 0.01	2.0 ± 0.2×10^5	0.18 ± 0.01
EspP	13.6 ± 3.0	311 ± 21	0.41 ± 0.03	0.060 ± 0.02	9.2 ± 0.2×10^3	0.51 ± 0.08
phoA	108 ± 11	310 ± 20	0.59 ± 0.03	0.18 ± 0.02	6.3 ± 0.4×10^4	0.45 ± 0.02
5A5L	63 ± 4	910 ± 50	0.42 ± 0.02	0.084 ± 0.003	1.1 ± 0.2×10^4	0.38 ± 0.02
8A2L	100 ± 5	≥2630	≥0.48	0.028 ± 0.003	5.6 ± 0.3×10^3	N.D.
Lucife-rase	130 ± 12	2060 ± 201	0.34 ± 0.02	0.039 ± 0.003	1.8 ± 0.3×10^3	0.65 ± 0.22

N.D.: not determined.

5.7 Supplementary Figures

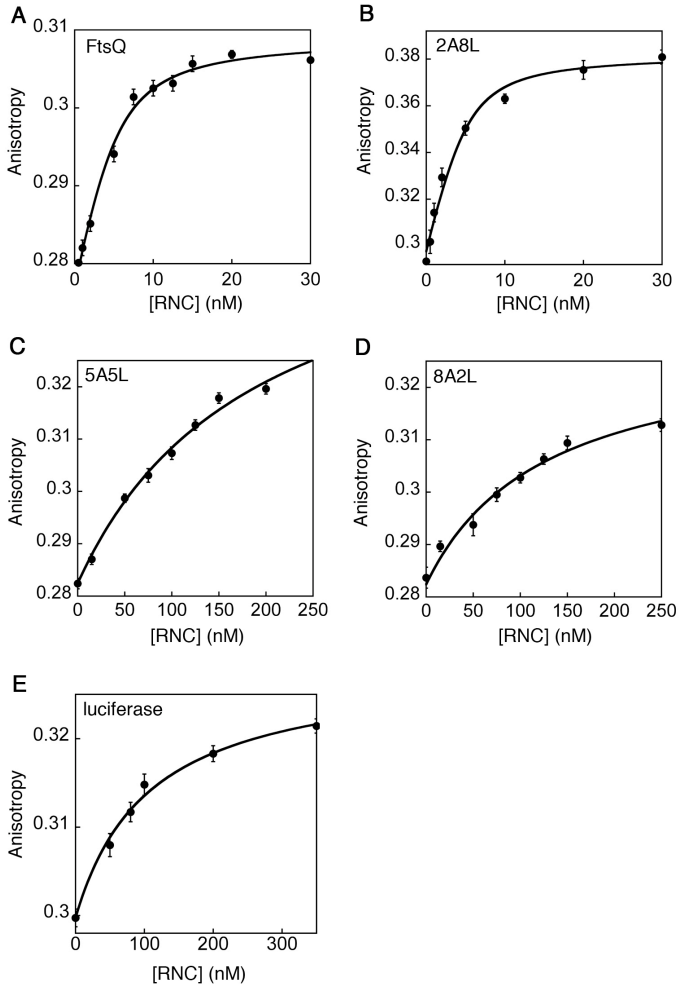

Figure 5.S1. The binding affinities of SRP for different cargos. Equilibrium titrations to measure cargo-SRP binding were carried out as described in the Methods. K_d values of each cargo (Table S1) were derived from quadratic fits of data according to Eq (5.3). Error bars are SDs from three independent experiments.

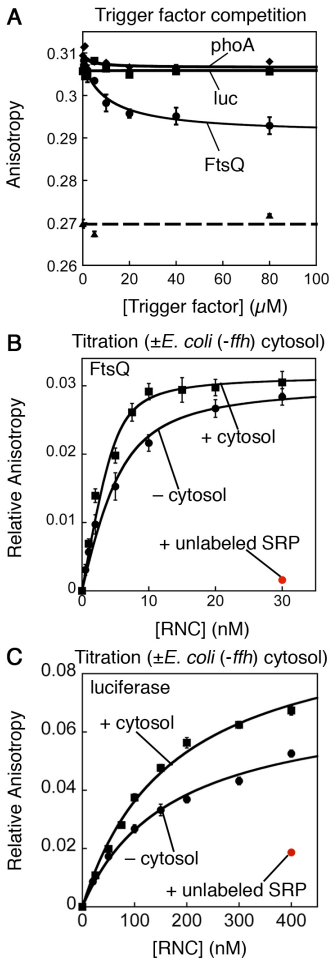

Figure 5.S2. Trigger factor and SRP-free *E. coli* (*-ffh*) total cytosol do not displace the SRP from the RNCs. (A) Fluorescence anisotropy of cargo-loaded SRP in the presence of increasing amounts of trigger factor. RNC_{FtsQ} (●), RNC_{phoA} (u) and $RNC_{luciferase}$ (■) are used as representatives of correct, weak and wrong cargos, respectively. The dashed line represents the anisotropy value of free SRP (▲). At each concentration, TF has been incubated with the RNC•SRP complex for sufficient time (15–30 min) to ensure that equilibrium has been reached. (B, C) Equilibrium titrations to measure the binding affinities of SRP for RNC_{FtsQ} (B) and $RNC_{luciferase}$ (C) in the presence (■) and absence (●) of SRP- and ribosome-free *E. coli* (*-ffh*) total cytosolic extract. Nonlinear fits of data to Eq. (5.3) gave K_d values of 0.10±0.02 and 0.67±0.11 nM for RNC_{FtsQ} with and without cytosol (B), respectively, and 174±14 and 170±10 nM for $RNC_{luciferase}$ with and without *E. coli* cytosol (C), respectively. In all titration experiments, fluorescence anisotropy changes can be competed away by unlabeled SRP (●). Error bars are SDs from three independent experiments.

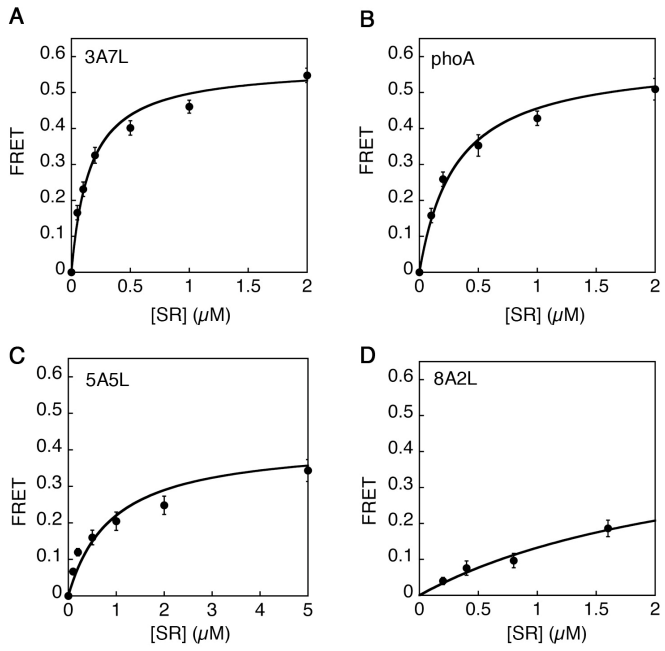

Figure 5.S3. Stabilities of the SRP•SR *early* intermediates formed with different cargos. Equilibrium titrations of the *early* intermediate were carried out as described in the Methods. Nonlinear fits of data to Eq (5.4) gave K_d values of the *early* intermediate in the presence of each cargo (Table 5.S1). Error bars are SDs from three independent experiments.

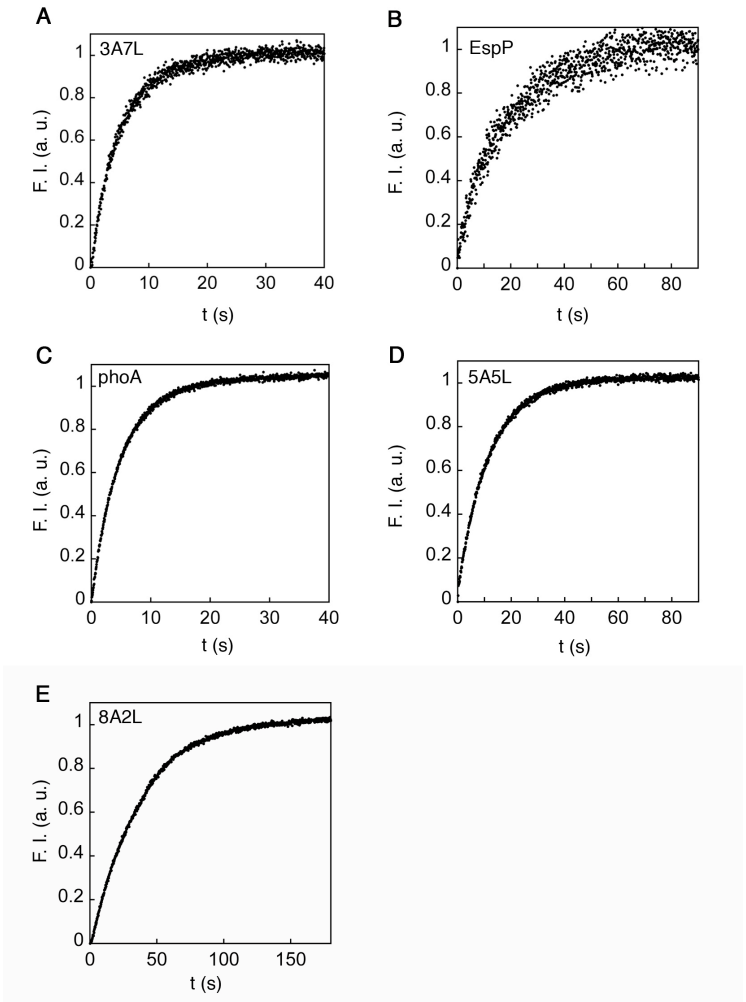

Figure 5.S4. The *early→closed* rearrangement is slower with weaker cargos. Rate constants of the GTPase rearrangements were measured using acrylodan-labeled SRP(C235) as described in the Methods. Rate constants with each cargo (Table S1) were derived from nonlinear fits of the data to Eq. (5.5). Reactions were carried out with 100 – 250 nM SRP, 200 nM RNC_{3A7L} and RNC_{EspP} or 500 nM RNC's with other signal sequences, and 50 –75 μM SR.

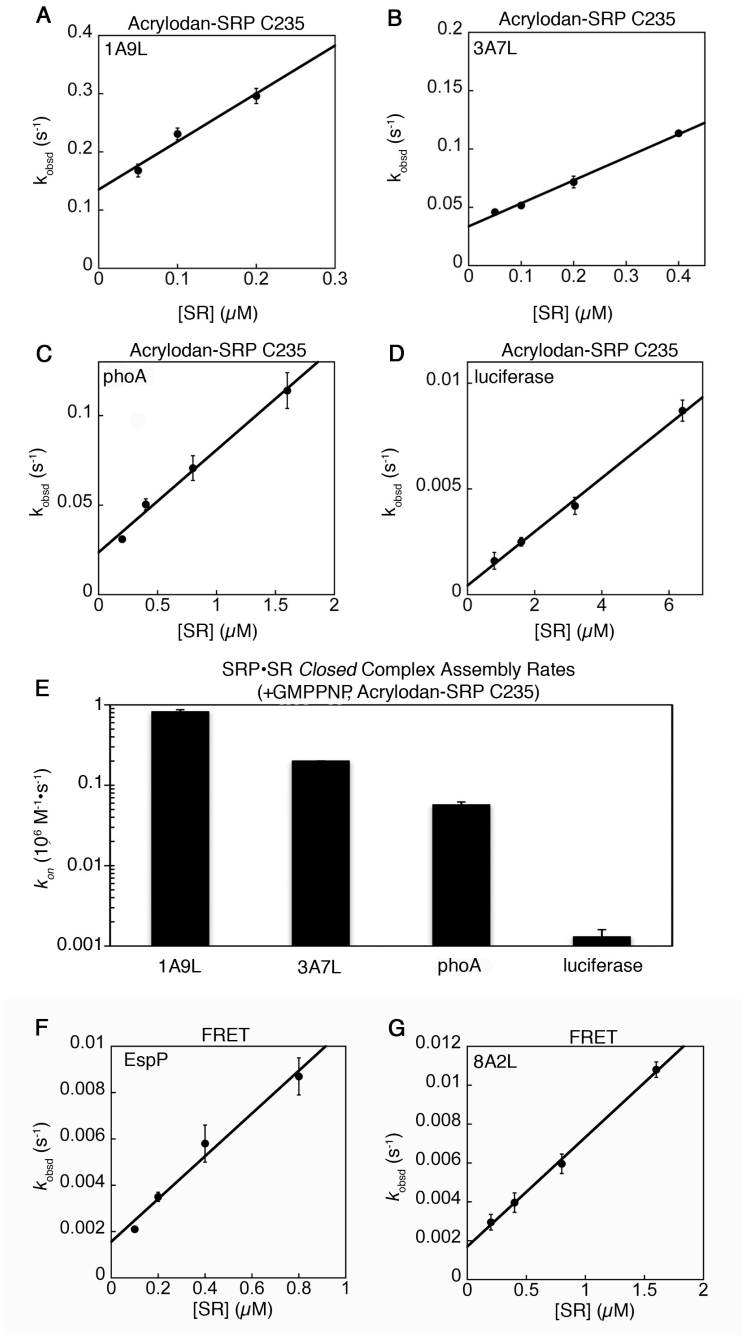

Figure 5.S5. Rate constants for assembly of the SRP•SR *closed* complex. (A-D) Complex assembly rate constants were determined using acrylodan-labeled SRP(C235) as described in the Methods. Linear fits of data to Eq (5.6) gave second order constants of complex assembly (k_{on}) of 0.82±0.05, 0.20±0.04, 0.057±0.005, and 0.0013±0.0003×10^6 $M^{-1}s^{-1}$ with RNC_{1A9L} (A), RNC_{3A7L} (B), RNC_{phoA} (C), and $RNC_{luciferase}$ (D) respectively. (E) Summary of *closed* complex assembly rates with different cargos measured by acrylodan-labeled SRP(C235). (F, G) Complex assembly rate constants for RNC_{EspP} and RNC_{8A2L} measured using FRET. Second order constants of complex assembly (k_{on}) were obtained from linear fits of the data to Eq (5.6) (Table 5.S1). Error bars are SDs from three independent experiments.

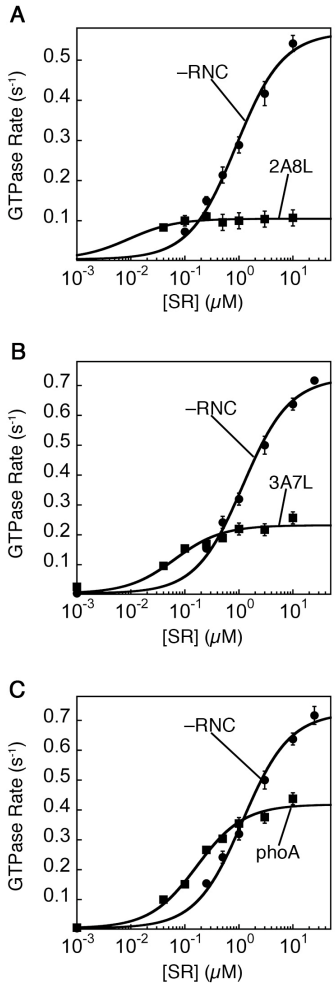

Figure 5.S6. Effects of different cargos on GTPase activation in the SRP-SR complex. GTPase reactions were carried out and analyzed as described in the Methods. GTPase rate constants (k_{cat}) from the cargo•SRP•SR complexes were obtained from nonlinear fits of data to Eq (5.7) (Table 5.S1). Error bars are SDs from three independent experiments.

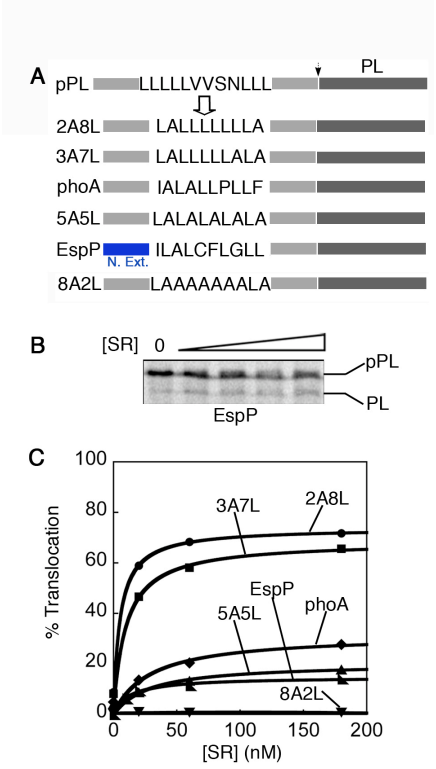

Figure 5.S7. Experimental determination of protein targeting efficiency of substrates bearing the different signal sequences. (A) Schematic diagram depicting the chimericpPL constructs used for the co-translational protein targeting assay (see Methods). The arrow between signal sequence (light grey) and mature protein (dark grey) shows the signal peptidase cleavage site from pPL. Blue denotes the N-terminal signal peptide extension of EspP construct. (B) SRP-dependent protein targeting and translocation efficiency of substrates with EspP signal sequences analyzed by SDS-PAGE. pPL and PL denote the precursor and signal sequence-cleaved forms of the substrate protein, respectively. (C) Quantification of the protein targeting and translocation efficiencies of each substrate tested.

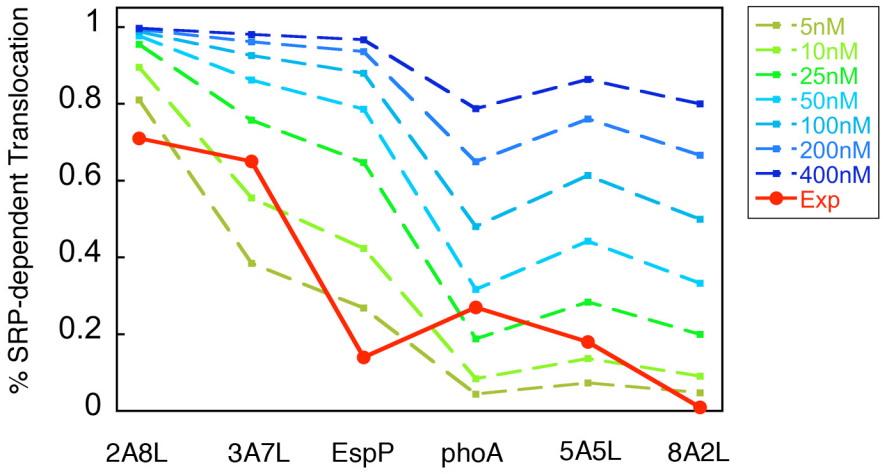

Figure 5.S8. Models based solely on discrimination in cargo-binding affinities would not reproduce the experimentally observed pattern of substrate selection by the SRP pathway. Numerical analysis for protein targeting and translocation efficiencies was carried out as described in the Methods assuming a one-step mechanism of substrate selection based on the binding affinities of SRP to different cargo substrates. Different effective concentrations of free SRP ranging from 5 to 400 nM (specified in the top right panel) were used. The red line depicts the experimentally determined protein targeting and translocation efficiencies (from figure 5.4C in main text) and was shown for comparison.

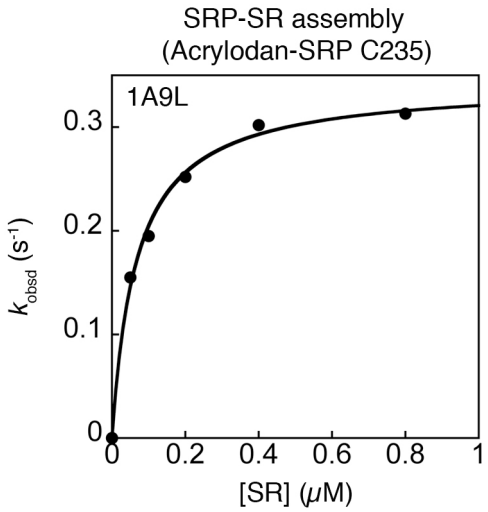

Figure 5.S9. Acrylodan-labeled SRP C235 monitors two-step assembly of the SRP-SR closed complex. Observed complex assembly rate constants were determined using acrylodan-labeled SRP(C235) as described in the Methods. The deviation from linearity of the observed rates indicate that assembly of the closed complex is a two-step process, with a unimolecular rearrangement rate-limiting at saturating SR concentrations. Nonlinear fits of data to Eq (5.7) gave the rearrangement rate from the early to the closed complex as 0.34 s^{-1} with RNC_{1A9L}.

5.8 Acknowledgments

We thank C. Schaffitzel and N. Ban for help with the purification of RNCs and trigger factor, J. Luirink for plasmids encoding the phoA signal sequence variants, L. Randall for the plasmid encoding luciferase, B. Bukau and E. Deurling for the plasmid encoding trigger factor, H. D. Bernstein for the strain HDB51, and R. J. Deshaies, A. Varshavsky, W. Zhong, N. Pierce, and the Shan laboratory for comments on the manuscript. This work was supported by NIH grant GM078024, career awards from the Burroughs Welcome Foundation, the Henry and Camille Dreyfus foundation, the Beckman foundation, and the Packard foundation to S. S.